

Your Interlibrary Loan request has been sent by email in a PDF format.

If this PDF arrives with an incorrect OCLC status, please contact lending located below.

Concerning Copyright Restrictions

The copyright law of the United States (Title 17, United States Code) governs the making of photocopies or other reproductions of copyrighted materials. Under certain conditions specified in the law, libraries and archives are authorized to furnish a photocopy or other reproduction. One of these specified conditions is that the photocopy or reproduction is not to be "used for any purpose other than private study, scholarship, or research". If a user makes a request for, or later uses, a photocopy or reproduction for purpose in excess of "fair use", that user may be liable for copyright infringement. This institution reserves the right to refuse to accept a copying order if, in its judgment, fulfillment of the order would involve violation of copyright law.

Interlibrary Loan Services: We Search the World for You...and Deliver!

Interlibrary Loan Services – FSU Community
James Elliott – Resource Sharing Manager
The Florida State University
R.M. Strozier Library
116 Honors Way
Tallahassee, Florida 32306-2047
Email: lib-borrowing@fsu.edu
Website: <https://www.lib.fsu.edu/service/interlibrary-loan>
Phone: 850.644.4466

Non-FSU Institutions:
Lib-Lending@fsu.edu
850.644.4171

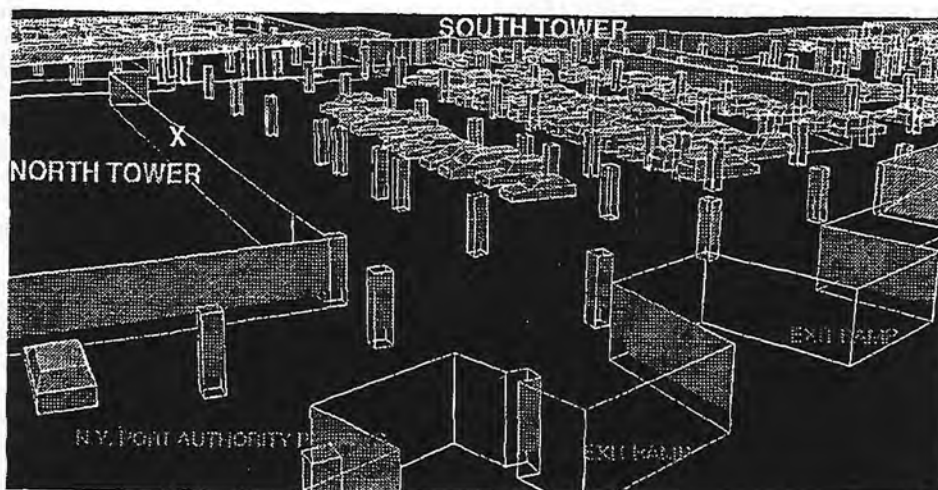
AIAA 95-0085

Numerical Simulation of Blast in the World Trade Center

Joseph D. Baum^{*}, Hong Luo^{*}, and Rainald Löhner^{}**

*** Science Applications International Corporation, McLean, VA 22102**

**** George Mason University
Fairfax, VA 22030**



**33rd Aerospace Sciences
Meeting and Exhibit
January 9-12, 1995 / Reno, NV**

NUMERICAL SIMULATION OF BLAST IN THE WORLD TRADE CENTER

Joseph D. Baum*, Hong Luo*
Science Applications International Corporation
1710 Goodridge Drive, MS 2-3-1
McLean, VA 22102

and

Rainald Löhner**
Institute for Computational Sciences and Informatics
George Mason University
Fairfax, VA 22030

ABSTRACT

This paper describes the application of FEFLO96, a recently developed three-dimensional, adaptive, finite element, edge-based, ALE shock capturing methodology on unstructured tetrahedral grids, to the simulation of blast diffraction inside the B-2 level of the World Trade Center garage. The ultimate objective of this study is to develop a simplified predictive methodology capable of defining the potential damage from a given HE load to a specific structure. Such a methodology can be used by law enforcement agencies charged with the prevention of and protection against terrorist attacks. As a first step in the development of this methodology, we simulated blast diffraction in the B-2 level. The geometry of the B-2 garage level was modeled as accurately as possible, based on the building blueprints. Included in the modeling were all the support columns and beams, access ramps, walls, stairways, retaining walls, and barriers. The simulation also included 284 vehicles, belonging to ten different size groups. The vehicles were parked at the correct parking location, in accordance with the garage parking blueprints. The computational domain (i.e., points, lines and surface definitions for the modeled geometry) was generated using a newly developed CAD-like solid-body generator (FECAD). The advancing front methodology (FRGEN3D) was then used to generate the surface and volume grids. The shock diffraction simulation was initiated using the results of a one-dimensional detonation code for a one thousand pound ANFO charge. The resolution and fidelity of the simulated shock wave diffraction phenomena, performed via a solution of the transient compressible Euler equations, were enhanced by the application of the classic H-refinement/coarsening grid adaptation scheme, with density as the critical adaptation parameter. A large number of shock waves was produced due to shock

diffraction around the walls, cars, and ramps. Excellent shock adaptation and resolution were obtained at all times. All shocks were captured as sharp discontinuities without producing pre- or post-shock oscillations. Several interesting 3-D shock diffraction processes were identified and discussed. Among these are shock diffraction processes, the formation of "hot spots" due to three-dimensional wave focusing at corners, shock reverberation within the parking level, and the formation of three-dimensional Mach stems.

INTRODUCTION

The evaluation of civilian structure vulnerability to terrorist attacks has become a timely and critical issue after the terrorist attack on the World Trade Center, and the failed attacks on other civilian targets in New York City. Since testing large structures for blast resistance is very expensive, and testing real targets is simply not practical, detailed numerical simulations offer a unique, accurate, and cost effective approach to assessing vulnerability of these structures to internal explosions.

The numerical simulation of an explosion within a confined environment requires simulating blast initiation and evolution, shock wave diffraction about many structural components, structural response to the blast, structural failure, blast transmission through open and/or fragmented walls, floors, and ceilings, multi-body response to the shock (e.g., vehicle translation due to shock loading), and determining the role of vehicle deformation in shock wave attenuation. This list indicates that methodologies from widely disparate fields such as computational fluid dynamics (CFD), computational structural dynamics (CSD), and material modeling must be combined to completely assess structure vulnerability to internal blasts. We have recently completed integrating our CFD methodology with DYNA3D, a state-of-the-art CSD methodology. Nevertheless, it was decided that for the first simulation it would be prudent to eliminate the structural coupling and treat all surfaces as rigid and non-responding.

*Senior Research Scientist, Associate Fellow AIAA.

*Research Scientist, Member AIAA.

**Research Professor, Member AIAA.

Over the past five years, we have devoted considerable effort to developing a general CFD modeling capability for the class of problems considered here. The objective of this effort was to create a numerical methodology capable of efficiently simulating transient shock-shock and shock-structure interactions for realistic, complex, engineering-type, three-dimensional geometries. Hence, the unstructured grid approach [1,2] was chosen as the most suitable for generating surface and volume grids for complex-geometry bodies. In addition, since the typical areas of interest require the simulation of both steady and transient strong shocks, a high-resolution monotonicity-preserving algorithm for unstructured grids was developed. The method, called FEM-FCT [2], is based on Zalesak's [3] generalization of the Flux-Corrected Transport (FCT) [4,5] algorithms to multidimensional problems. Extensive applications of FEM-FCT to 2-D [6] and 3-D simulation [7-10] have demonstrated excellent agreement with experimental data. With these schemes, both traveling and stationary shocks are captured within two-three gridpoints (for either 2-D or 3-D) without the over- and undershoots that appear in linear schemes. Finally, since the flowfields are typically smooth (except for a few regions where strong gradients appear), efficient adaptive refinement techniques for transient problems are required.

We have recently developed high accuracy schemes on unstructured grids using an edge-based data structure. The edge-based data structure significantly improves the efficiency of the algorithms by reducing memory requirements by about a factor of 2.5 to 3.0, and CPU requirements by about 2.5. In addition, the scheme enables a straightforward implementation of upwind schemes in the context of finite element methods. An extended discussion of constructing various upwind and central difference schemes and their applications to steady and transient simulations is given in Refs. [11-13]. Several numerical experiments were conducted with both an edge-based FEM-FCT algorithm and an edge-based second-order Roe upwind finite element scheme. Both numerical algorithms utilized adaptive H-refinement. The results demonstrated [11] that the second-order Roe upwind finite element scheme produced better results for steady flows. Nevertheless, for transient flows, the FEM-FCT methodology produced better results, at computational costs about 75% to 80% lower than the second-order Roe upwind finite element scheme. Hence the clear choice of the FEM-FCT methodology for the present application.

THE NUMERICAL METHODOLOGY

Experience gained over the past three years in the generation of surface and volume meshes for the simulation of flows about such complex geometry structures as airplanes, tanks, trains, cars and trucks [7-10,14], has shown that once the surface and volume mesh generation has been automated, the surface description (i.e., point, line and patch definition), as well as the correct definition of boundary conditions, become the dominant man-hour bottlenecks. This information led

to the development of FECAD, a suite of efficient, user-friendly utilities that allows the quick production of FRGEN3D-compatible, error-free input. In addition to basic CAD-CAM operations (shrinking, translating, rotating, surface lofting, etc.), FECAD also eases the merging of several surface parts into one cohesive, well-defined input-file. This allows the merging of files produced by different users and/or different surface generators. Most importantly, FECAD allows graphical interrogation of the surface data, and has many built-in diagnostics to avoid undesirable features such as doubly defined points, isolated points or lines, badly defined lines or surfaces, and lines or surfaces that are directed incorrectly. FECAD also allows the specification and visualization of boundary conditions, saving the user many error-prone hours during the later stages of a run. FECAD has proven to be an invaluable aid when trying to construct an error-free FRGEN3D-compatible input file in a matter of days or even hours.

In order to specify the desired element size and shape distribution in space, a combination of background grids [15] and sources [16] is employed. While the specification of sources is relatively simple using an interactive graphical interface, the generation of background grids is more complex. For this reason, we developed PREBACK, a semi-structured 3-D background generator. Experience with the user community has shown that the preferred method of generating background grids is by lofting a 2-D triangulation into the third dimension, or simply by rotation. PREBACK allows both of these operations. In addition, it allows interactive operations to move background grid-points around (translations, rotations, shrinking, etc.), as well as allowing the user to modify the grid-generation parameters (size, shape) in space.

The mesh used for the present calculations was generated using FRGEN3D [15,16]. This unstructured grid generator is based on the advancing front method. After defining the surface of the domain to be gridded, the surfaces are triangulated. Thereafter, the face that forms the smallest new element is deleted from the front, and a new element is added. This process is repeated recursively until no more faces are left in the front. FRGEN3D generates approximately 50,000 tetrahedra per minute on a Cray-YMP. This number may increase for smaller meshes (less than 50,000 tetrahedra), as more of the front collapses per element generated. For very large meshes, a global H-refinement option is available. With it, the rate of generation is increased to about 400,000 tetrahedra per minute.

The flow solver employed was FEFLO96, a new 3-D ALE edge-based hydro-solver based on FEM-FCT [2,5,11-13]. H-refinement is the preferred approach for grid adaptation [17,18]. The high order scheme used is the consistent-mass Taylor-Galerkin algorithm. Combined with a modified second order Lapidus artificial viscosity scheme, the resulting scheme is second order accurate in space, and fourth order accurate in phase. The spatio-temporal adaptation is based on local H-refinement, where the refinement/deletion criteria is a modified H2-

seminorm [17,18]. The critical parameter for the refinement/deletion criteria is density.

Post-processing was performed with the FEPOST3D and FEMOVIE packages. FEPOST3D is based on FEPLT4D [19], but performs all CPU-intensive filtering operations on the Cray. Only the plane or surface triangulations are sent back to the graphics workstation for plotting. The user specifies the planes and surfaces to be inspected before the run. Although seemingly trivial, this step has significantly reduced data transmission and post-processing time, as one deals with about 27 Mbytes of ASCII information, compared to about 720 Mbytes of binary data for a complete flowfield mesh. These smaller data sets in turn allow for quick and efficient movie production from hundreds of frames.

NUMERICAL RESULTS

The methodology described above was applied in this research effort to simulate blast wave diffraction within the B-2 level of the World Trade Center. The scenario modeled here assumes that a bomb was hidden in a vehicle that was parked and detonated at the curb of the northbound exit lane to West Street, near the south wall of the WTC's north tower. As noted above, this simulation is only the first step in a comprehensive research effort directed at developing a complete methodology for the prediction of blast damage to civilian structures. The ALE algorithm employed here can simulate the structural response (i.e., motion) to the blast. Nevertheless, since this effort is only the first step in the methodology development, we defined all walls as "hard walls," i.e., all impacted surfaces were specified as non-responding, an assumption that will be relaxed in future computations.

1. Solid Body Definition

In the absence of CAD data (the latest blueprints are from 1968), the complete B-2 level geometry had to be reconstructed from blueprints, not a trivial task considering the complexity of the structure. All wall locations, ramps, exhaust plenum spaces, mechanical rooms, stairways, toll booths, curbs, A/C, and supply and elevator shafts were modeled as accurately as possible from the structural and architectural drawings.

The solid body definition was aided by our FECAD methodology. Several special routines were developed during this research effort to aid in the construction of the structure. For instance, we developed a special module to quickly place all cars in their exact parking space, as marked in the parking map. First we had to create a library of car CAD definitions. We therefore measured the pertinent dimensions of cars in our own parking lot representing ten typical car groups. We included a small passenger car (Hyundai), a mid-size passenger car (Chevy Cavalier), a full-size sedan (Ford Taurus), a full-size station wagon (Ford Taurus wagon), a small sport utility vehicle (a basic Jeep), a small pick-up (Dodge Ram), a large sport utility vehicle (Ford Explorer), a large pick-up (Ford F-150), a minivan (Dodge Caravan), and a full-size van (Ford). Next

we created a line and surface definition for each vehicle. Since the available information indicated that the parking garage was full at the time of the explosion, we filled all available parking spaces. These were defined exactly using the parking plan, by creating a single location marker per parking space (the coordinates where the back center of the vehicle should be placed), and a vector (the parking direction). Next we developed an algorithm that randomly distributed the cars belonging to the ten groups within all available parking spaces. We recognize that the low ceiling makes shock diffraction about each vehicle critically dependent on its top clearance (i.e., vehicle height). Therefore, placing the vehicles in their actual parking space could be vital to correctly predicting shock diffraction and shock loading. Unfortunately, this information was not available. All vehicles, including the burned-out, moderately and even slightly damaged, were towed away before a survey of damage and vehicle identity was conducted. Hence the randomly distributed parking arrangement.

The line description for the complete configuration definition, which included 5397 points, 8781 lines and splines, and 3750 surfaces, is shown in the Fig 1a view from north of the north tower. In the following discussion, we will interchangeably refer to the north tower as tower A, and the south tower as tower B. Two areas were not modeled in this simulation. These are the New York State parking area south of tower B, including the adjacent Governor's parking east of tower B, and the large parking area located north of tower A. These parking areas were not modeled, since vehicles parked there did not sustain any observable damage. The low damage level, and by implication, the low shock loading, was due to blast wave attenuation because of the long distance from the blast point, and the additional shock diffraction about a 90° corner that was required for the incident shock to reach these areas.

Once we had collected all the geometric data from sources such as architectural, structural and parking blueprints, the generation of the solid body definition took less than five working days. The time required to perform this task was tremendously shortened by the interactive capabilities built into our FECAD methodology. Once all of the surfaces were defined, the generation of the surface and volume meshes was completely automatic, an important advantage of the advancing front algorithm [15]. The grid generation can be performed either interactively on a workstation, or remotely on a Cray. Generating such a grid with a current multi-block structured grid methodology would have taken significantly longer.

Figure 1b shows a view of the solid surfaces as viewed from the north. Note the clear definition of the cars, columns, walls, the ramp down to B-3, referred to in the blueprints as ramp T (near tower B), and the ramp up to B-1 (on the right), called ramp N. The group of rooms south of ramp T includes A/C, elevator and transfer shafts, a toll booth, an enclosed stairway, an elevator shaft, and a mechanical room. Adjacent to tower B are three elevators with an elevator lobby,

and an A/C shaft. While the tower walls and the various room walls are the actual walls, the walls on the circumference are masonry walls forming an exhaust plenum with the real garage walls. In Fig 1b, all surfaces below 25.0 cm were eliminated, simply to delete the floor from the pictures.

Figures 1c and 1d show the central parking zone as viewed from the east (Secret Service parking zone) and the west (NY Port Authority parking), respectively. "X" marks the approximate blast point. Shown in the Secret Service area are the ramp down, referred to as Ramp S, which leads down by 4.75 ft, a walled enclosure on the left, which is the upper wall of the PATH train mezzanine (PATH is the commuter rail service), and a walled stairway at the center. The two presidential limousines are located to the right of the center, enclosed in two side walls. Since the ceiling above the Secret Service area was only seven inches thick, compared with eleven inches elsewhere, support beams (one foot wide) were constructed between all columns.

Finally, Fig 1e shows the west side of Tower A, with a telephone room (adjacent to tower A), an enclosed plenum (to its left), the NY Port Authority chauffeur office (left, bottom corner), and the adjacent limousine parking area. Also shown here, as well as in Fig 1d, are ramp B, the northbound exit to West Street, and to its right, ramp A, the southbound exit to West Street.

In an effort to better understand the complex three-dimensional shock diffraction physics, we produced a video that viewed the shock evolution within the B-2 level from different angles. The first segment of the video attempts to visualize, via a fly-through, the complex geometry structure. This video constitutes a stepping stone in our virtual reality methodology development efforts. The ultimate objective of this effort is to ease current difficulties in understanding complex 3-D shock diffraction processes. Two snapshots (out of several thousand) taken during the fly-through are shown in Fig 2. In the fly-through, the camera entered the B-2 level through ramp B, the northbound exit to West Street, and traversed the exit lane where the explosive-laden vehicle was parked near the south wall, with the central parking to the right. Figure 2a shows a section of this parking area. The snapshot shown in Fig 2b is taken as the camera traveled down ramp S to the Secret Service area, and approached the two presidential limousines.

2. Problem Initiation

Blast initiation assumed a vehicle parked near the right curb of the exit lane, leading to the northbound exit to West Street (ramp B). This scenario places the vehicle a distance of 10 feet from one of the main support columns of tower A. The initiation assumed a charge of a one thousand pounds of ANFO HE. The blast was initiated as a point source (the easiest, though certainly not the best assumption) placed on the garage floor, and propagated the blast wave until it was only a short distance from the south wall of tower A. As a consequence of the point-blast initiation, higher pressures on the ceiling than on the floor should

be expected later on in the simulation, as the flow stagnates on the ceiling while propagating parallel to the floor.

3. Shock Wave Diffraction

The numerical simulation of shock diffraction within the B-2 floor of the World Trade Center is especially suited for an adaptive refinement methodology. The large dimensions of the computational domain (20,249 cm long, 17,743 cm wide, and 580 cm high) are in contrast to the requirement to model the shock as a sharp discontinuity (or at least, minimize shock thickness), and model the smallest physical features of interest (i.e., while modeling the complete domain, also model shock diffraction about a wall that is less than 20 cm thick, a ratio of 1:1000). These contrasting requirements can be fulfilled only by using an adaptive methodology. Still, some compromises on mesh size and total number of nodes had to be made. When the simulation was initiated, the largest memory supercomputer available to us was a Cray C-90, with 128 MWords static memory. In an effort to optimize flow resolution within the limited available memory, we initiated the simulation by modeling only the zone fairly close to blast point. This area borders to the north, the south wall of tower A; to the south, the row of columns north to Ramp T; and to the east and west sides it extends the width of tower A. In addition, we allowed only two levels of refinement. Thus, the initial mesh before refinement had only about 370k points and 1.95 million elements. At $t=25.7$ ms, when the leading shock was close to the boundary of the modeled domain, we remeshed, modeling a larger portion of the B-2 floor. We then interpolated the solution from the old mesh to the new mesh, adapted twice (two levels of refinement), and continued the computation. By this time we gained access to a Cray YMP/M-92 supercomputer with 256 MWords static memory, so our initial mesh size was about 780K points and 4.1M elements. The second mesh extended all the way to the walls on the east and west sides, to the south side of the PATH wall on the north, and to the north wall of tower B to the south. Finally, at $t=108.9$ ms, we generated a third mesh that included the complete domain. The initial mesh included about 1.54M points and 8.0M elements. After solution adaptation, the final mesh included about 3.52M points and 18.1M elements. This part of the simulation was executed on a new Cray YMP/M-92 with 1 GWords static memory.

Past experience with this class of problems indicates that the following choice of refinement and coarsening parameters produces the best results: refinement tolerance: $CTORE=0.20$; coarsening tolerance: $CTODE=0.08$; noise parameter: $\epsilon=0.05$; key variable: density; refinement frequency: every 5-7 timesteps; number of protective layers: none; and Courant number of the hydro-solver: $C=0.35$.

Pressure contours at several times are shown in Figs 3 through 9. Results are shown on the surfaces only, since plotting volumetric data is too confusing. Due to the wide range of pressure amplitudes modeled

here (as is the case for all decaying blast wave simulations), and to avoid highlighting instantaneous pressure spikes due to wave interaction and focusing, pressure contours are shown within a pressure range from the minimum to $0.33 \times \text{maximum}$ (experience-derived value). The gouraud shaded pressure plots use 256 colors, with blue representing the lowest pressure, increasing pressure through cyan, green, yellow, and red, to magenta, which represents the highest pressure. All pressure values above the thirty-third percentile of the maximum value will be painted magenta. On all figures, the indicated maximum pressure value is only one-third of the real maximum value. Hence, all pressures colored magenta have up to three times the indicated maximum pressure.

The sequence of pressure contour snapshots shown here is included to help understand the complex, multiple shock evolution processes. Much better understanding can be gained by carefully analyzing the video data, which includes 1459 dumps. Unfortunately, these data cannot be included in the limited space allocated here. Tremendous insight into shock physics is gained by simply tracking the evolving shocks from one time step to the next. These results also demonstrate the ability of the adaptive methodology to capture and define, in great detail, any single shock diffraction process, such as shock diffraction about a single column, while still simulating flow evolution within the complete computational domain.

The maximum pressure amplitude observed when the initial shock reflected from the ceiling was above 25 kpsi. At $t=0.175$ ms, the shock impacted the south wall of tower A, an unsupported cinder block wall. Although the wall probably failed a very short time after shock impact (with an amplitude of about 8 kpsi at this time), it did not move a significant distance until much later.

Strong shock wave focusing at the wall corners is observed at $t=1.75$ ms. The higher pressure amplitude obtained at the ceiling corner than at the floor corner resulted from the initiation as a point blast on the floor. Thus, the shock at the floor level is reflected as a one-dimensional reflection, while the top shock experienced a 2-D wave focusing at the corner. The higher stagnation pressure persists for a long time, as shown in Fig 3a at $t=3.63$ ms. Since the blast was initiated on the floor, pressure data on the wall at a later time (Fig 3b at $t=5.25$ ms) should show the shock near the floor propagating ahead of the shock near the top, as observed initially. However, the higher stagnation pressures at the ceiling corner resulted in the formation of a three-dimensional Mach stem, and hence, higher shock velocity near the ceiling than near the floor. Also observed at this time ($t=5.25$ ms, Fig 3b) is the impact on the floor of the shock reflected from the wall's top corner.

The first of many shock diffraction processes about columns is also shown in these figures. The incident shock impacted the two closest columns at $t=2.6$ ms. Analysis of the results at $t=3.63$ ms (Fig 3a) shows shock diffraction about the column, with the higher

reflected pressure amplitudes at the side facing blast point. Since the solution was initiated as a point blast on the floor, and since this column is currently impacted by the direct shock and not the reflected shock from the wall, the shock arrives later with increased height. The shock has already diffracted about the column at floor level, while at ceiling level it has just impacted - hence the higher pressure amplitudes near the ceiling.

The leading shock impacts on the side corner wall of the north tower at $t=7.0$ ms. Due to the higher pressure amplitude and shock propagation velocity near the ceiling, the initial impact point on the corner is at the ceiling. The large pressure amplitude at the corner due to shock wave focusing will result in a reflected shock with a significant pressure amplitude, as observed at $t=12.51$ ms (Fig 4a). The results at this time also highlight some interesting shock diffraction processes about cars and columns, which, coupled with the sharp, non-oscillatory capturing of all shocks in the system, demonstrate one of the most important advantages of the adaptive refinement methodology: the ability to clearly and accurately represent the smallest-scale physical processes, while simultaneously modeling the large scale phenomena. Most shocks in the domain, strong and weak, were captured over two elements, even after many thousand time steps. Examination of the leading shock at $t=12.51$ ms shows on the right (east) the diffracted wave about the southeast corner room of tower A, and shock diffraction about a column. Closer to the center of the domain we observe a nicely detailed shock diffraction about a column, with almost symmetric rarefaction waves on both sides, and a reflected shock upstream of the column. A similar diffraction process is observed about a column toward the left of the expanding shock. Shock diffraction about the cars situated between these columns is more complex. The reflected pressure amplitude depends on the car profile (i.e., percentage of blocked area from floor to ceiling), car width, and shock incident angle. The impacting shocks were partially transmitted under the cars (wheels were not modeled here). In addition to the effective area blocked by the car, the strength of the transmitted shock front depends on shock reverberation between cars. Examination of the solution at a later time (Fig 4b at $t=19.49$ ms), shows the recovery of the leading shock front expanding at the center, with reflected shocks upstream of the cars and columns. Notice: a) For the column on the north side of ramp S (down to the Secret Service area), the shock is about to impact on the column at floor level, while it had already reflected at the ceiling, indicating a higher shock velocity near the top; b) Of the left two columns near the south wall already traversed by the shock, the diffraction about the column closer to blast point at this time shows that: 1) the direction of the rarefaction waves is away from the second column, not away from the blast; 2) the strength of the reflected shock is higher away from the second column; and 3) the pressure contours on the first column side facing the blast source show an expansion, not a reflection. This

indicates that at this time the flow about this column is influenced more by the reflection from the adjacent column than by the primary shock; and c) While the primary shocks at this time are clearly the blast shock and the reflected shock from the corner, a second front expanded radially, *cocentric with the primary shock*. This is the reflected shock from the wall/ceiling corner (also shown in Fig 3b at $t=5.25$ ms).

A second larger mesh, encompassing a larger domain, was generated at $t=25.8$ ms. The solution was then interpolated from the first mesh to the second, and adapted twice. The minimum mesh size, after adaptation, was almost identical to the minimum size obtained in the first mesh. Figure 5a at $t=29.03$ ms shows the larger zone. The shock has just diffracted around the southeast corner of the tower A. A single shock is propagating at this time from right to left (i.e., west-bound) along the south wall. A second shock, propagating eastbound, is only visible at $t=34.45$ ms (Fig 5b). After a careful analysis of the video data, we concluded that this shock is the reflection of the primary shock from the two columns and cars on the center-left side, discussed in the paragraph above ($t=19.49$ ms). The interaction of the two shocks produced the high pressure zone shown at the center of the wall in Fig 5b ($t=34.45$ ms). On the east side, the primary shock descended to the Secret Service area at $t=39.9$ ms, while on the west side, the shock is about to expand into the NY Port Authority parking area.

Complex shock diffraction processes are observed at $t=59.48$ ms (Fig 6). The incident shock expanded behind the southwest corner of tower A into the NY Port Authority area, an expansion modified by a nearby column. The reflected shock from this column is observed on the south wall of tower A. Also observed on this wall are the two reflections discussed in the previous paragraph, with a significant peak pressure increase for the eastbound-propagating shock wave. Frame-by-frame analysis of the video data shows that shock amplitude increased at this time due to its interaction with a reflected shock from the corner moving in the opposite direction. Incidentally, the second shock is the oblique reflection of the incident shock from the first row of cars. These shocks, as well as many others, are hard to identify in these figures due to the choice of pressure scales, but are easily identified when plotting the results on a reduced pressure range. Several shock diffraction processes are identified on the west (left) side. These include, from north to south: a) the shock approaching the West Street exits (ramps A and B); b) the shock impacting the northern corner of ramp B; c) the reflected shock from the wall separating the two exits; d) the reflected shock from the column upstream of this wall; e) shock impact and reflection from the southern corner of ramp A; f) the sharply captured primary shock about to impact ramp N (leading upstairs); g) shock reflection from the column just ahead of ramp N; and h) the oblique shock reflection from the second row of cars, moving in a northwest direction. At the center the incident shock approaches the north wall of ramp T. At the center-right of the domain we observe: a)

Dual shock waves between ramp T and the cars parked to the west of tower B: the incident shock followed by the curved reflected shock from the southeast corner wall of tower A. The higher amplitude portion of this shock propagated unperturbed in the north-south corridor between the columns of cars. Its western portion was significantly diffused by diffracting about the column of cars parked on the left side of the traffic lane; b) Shock reflection from the row of cars parked near the west wall of the tower B. These cars were broad-sided, hence the large amplitude reflection; and c) Shock reflection from the northwest corner rooms of tower B. In the Secret Service area we observe the shock reflection from the first row of beams, and the weakening of the front pressure amplitude as the wave expands to the north.

The dominant shocks on the west (left) side at $t=89.55$ ms (Fig 7a) and $t=95.81$ ms (Fig 7b) are the shock reflections from the walls of ramps A and B, shock reflection from the second row of cars (moving in a northwest direction), and shock reflection from the wall of ramp N. The primary shock was partially reflected from the side wall of ramp N, and the row of cars north of ramp T, expanded around the wall surrounding ramp N, and about the vehicles parked west of ramp T. The front propagating south shows (Fig 7b), from left to right: a large amplitude shock and a Mach stem formed near the west wall (between the wall and the adjacent cars); a lower amplitude shock diffracting about the parked cars; the incident, large amplitude shock in the traffic lane, followed closely by the reflection from the side wall of ramp N; the broad-side impact of this reflected shock on the row of cars north of ramp T; shock diffraction about the southwest corner of ramp T; and the impact of the shocks reflected from ramps A and B on the central two rows of cars and on the row of cars north to tower N. Naturally, each shock impact produces a reflected shock, plus an assortment of shocks that reverberate between the cars. Notice, for instance, the large amplitude reflection of the primary shock from the car parked directly west (behind) of ramp T. In the center the dominant shock is the reflected shock from the wall of ramp T. Shock stagnation at this wall produced a fairly high pressure amplitude, which explains the significant damage to the cars parked nearby, and the collapse of the wall. The results at this time ($t=95.81$ ms) show the complexity of this reflected shock. Since the cars to the left (west) and at the center of the wall are parked normal to the wall, the shock front is fairly uniform. On the right (east), however, the two vehicles parked diagonally perturbed the flow sufficiently to produce a curved (almost spherical) reflected shock.

At the center-right, we observe the sharp shock transmitted in the traffic lane between ramp T and the west wall of tower B, the multiple reflections from rooms near the northwest corner of tower B, and from the broad-sided parked cars. Due to the pressure scales chosen for plotting the contours, the reflected shocks from the northwest rooms are temporarily invisible while they propagate in a northwest direction toward

the south wall of tower A. At $t=108.85$ ms and later, we observe the interaction of these waves with the weak shock traversing the south wall (waves discussed previously), which gives rise to higher pressure amplitudes. The primary shock diffracts into ramp T at $t=76.99$ ms, and about its southern wall at $t=89.55$ ms. At $t=95.8$ ms (Fig 7b), the sharp, non-oscillatory captured primary shock, diffracts about the south wall of ramp T and the transfer shaft room near the west wall of tower B. The reflected shock from the north wall of ramp T expands at this time near the ramp entrance.

In the Secret Service area, we observe the evolution of the primary curved shock and note the multiple diffraction processes about the columns. The shock reflected from the two central columns at $t=89.55$ ms (Fig 7a) and interacted at $t=95.81$ ms (Fig 7b) with the walls of the pipe room attached to the north wall of tower B, to produce a strong reflection, an expansion, and a Mach stem. The weakened incident shock expanded to the north, and hit the PATH wall at $t=106$ ms. The shock front impacted the presidential limousines at $t=115.91$ ms. The results at $t=95.81$ ms show near the north wall of tower B a reflected shock and a spherical reflection with a circular imprint on the floor. Shock wave reflection from a corner of the support beams produced this large amplitude spherical reflection.

The shorter distance between the east traffic lane (the lane between tower B and ramp T) and blast point resulted in more energy initially transmitted through this lane than through the west traffic lane (between the west side of ramp T and ramp N). Hence, at $t=158.73$ ms (Fig 8) we observe the dominance of the east-diffracted shock. At later times we observe higher pressures and more energy behind the west-propagated shock. At $t=158.73$ ms, the east shock progress was partially delayed due to shock diffraction about the cars adjacent to the tower B west wall. Several weakened shocks emerge after diffracting about the many columns and rooms. The west shock includes two waves: the leading lower amplitude incident shock, followed closely by a group of higher amplitude reflected shocks. Note that this is not a diffused shock, but two separated shocks. After diffracting through two rows of parked cars, the weakened front, still looking sharp even with an amplitude of about 1.5 psi, reached the south wall at $t=287.73$ ms (Fig 9). The west shock continued to expand, but still lagged behind. The higher pressure amplitude wave slightly lagged behind at $t=251.18$ ms, and finally caught-up with the weaker front shock at $t=269.49$ ms.

In the Secret Service area, the reflected shock from the north wall of tower B propagated north, and impacted the PATH walls at about 220 ms. Notice that the loading is on the southern and western walls of the PATH structure, the walls that failed in the blast. Shock reflection from the eastern wall of the WTC is observed at later times. Analysis of the actual damage to the eastern wall (an unsupported masonry wall) shows that the wall failed from the tower B corner to the south, to as far north as the car parking area south

of the PATH wall. The numerical results indicate that the undamaged wall experienced lower shock loading due to shock diffraction about the PATH structure, and the flow blockage due to the high density parking just south of the PATH wall (three rows of cars, parked fairly dense, including several large pick-ups). Finally, damage analysis shows masonry wall breach at the north wall of tower B, on both sides of the pipe room. These results can be easily explained by the fact that the pipe-room protrusion resulted in flow stagnation, and hence a strong reflected shock, for either the incident wave or the reflected wave from the east wall.

Computational Resources Expended

The solution was integrated for about 13,900 time steps, and was conducted in three steps, as explained previously. The first stage took 5,300 time steps, and consumed approximately 8 CPU hours, single processor, on a Cray C-90 at Cray Research Inc. and NASA Ames Research Center. The second stage took 3,400 time steps, and consumed approximately 52 CPU hours, single processor, on the much slower Cray YMP/M-92 at Cray Research Inc. The third stage took 5,200 time steps, and consumed approximately 135 CPU hours, single processor, on a slower Cray YMP/M-92 at the Arctic Region Supercomputer Center, University of Alaska, Fairbanks, AK.

At the latest stages of the computation, a typical refined mesh size in this computation was approximately 7 cm, using two levels of refinement. Considering the huge dimensions of the gridded domain, which has a length of 20,249 cm, a width of 17,743 cm, and height of 580 cm, employing a fixed-grid mesh with identical resolution would have required a mesh of about 609 million elements, a mesh too big even for current generation supercomputers.

SUMMARY AND CONCLUSIONS

This paper described the application of a recently developed three-dimensional, adaptive, finite element, edge-based, ALE shock capturing methodology on unstructured tetrahedral grids (FEFLO96) to the simulation of blast diffraction inside the B-2 level of the World Trade Center. The scenario modeled here assumed that an explosive-laden vehicle was parked and detonated near the curb on the street exit lane, on the B-2 garage level.

The resolution and fidelity of the simulated shock wave diffraction phenomena, performed via a solution of the transient compressible Euler equations, was enhanced by the application of the classic H-refinement/coarsening grid adaptation scheme, with density as the critical adaptation parameter. A large number of shock waves was produced due to shock diffraction around the walls, cars, and ramps. The evolution of the primary shock and the multitude reflections were studied in great detail. Several shocks were tracked over time. In addition, the observed actual damage was correlated with the observed numerical predictions. Several interesting 3-D shock diffraction processes were identified and discussed. Among

these are the formation of "hot spots" due to three-dimensional wave focusing, shock reverberation between cars, shock diffraction about cars and columns, and the formation of three-dimensional Mach stems.

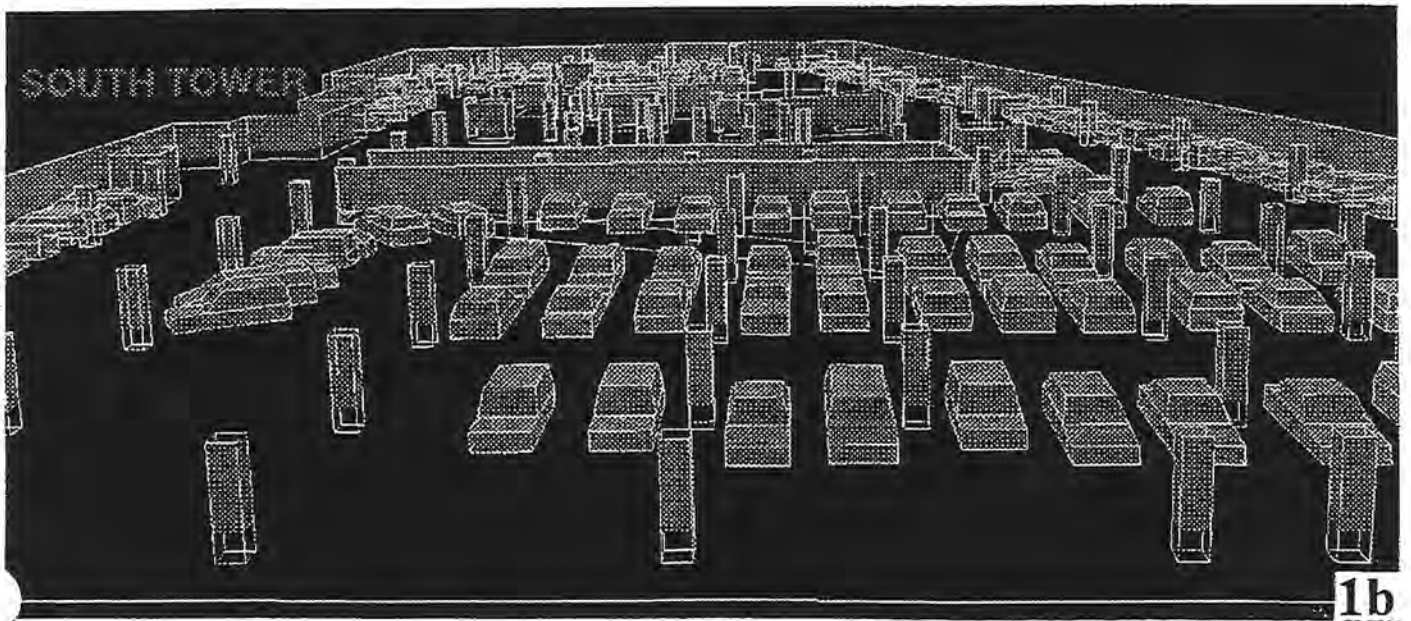
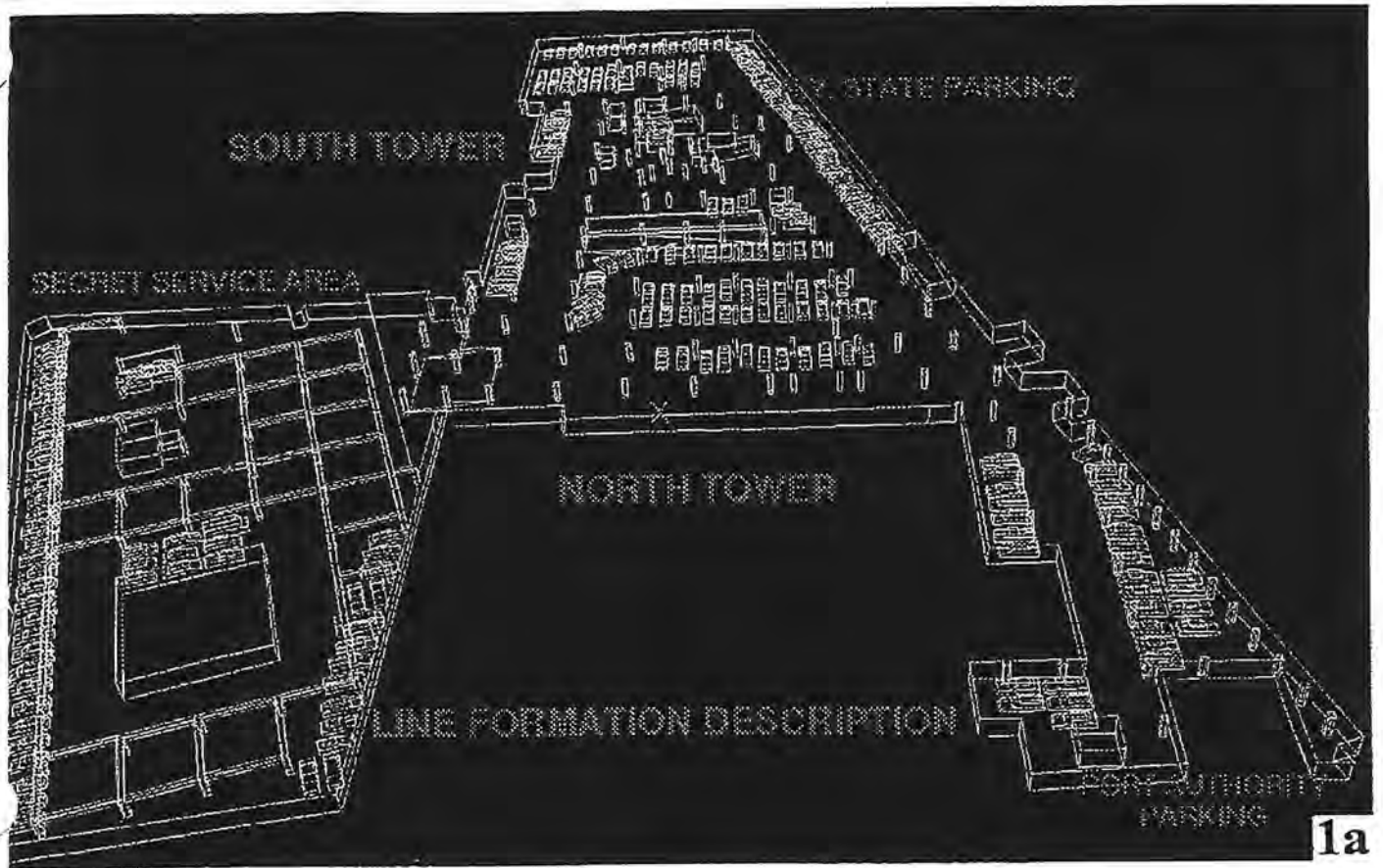
The computational results obtained demonstrate the successful application of the new 3-D adaptation procedure to shock diffraction about hundreds of complex-geometry structures. Excellent shock adaptation and resolution were obtained at all times. All shocks were captured as sharp discontinuities without producing pre- or post-shock oscillations.

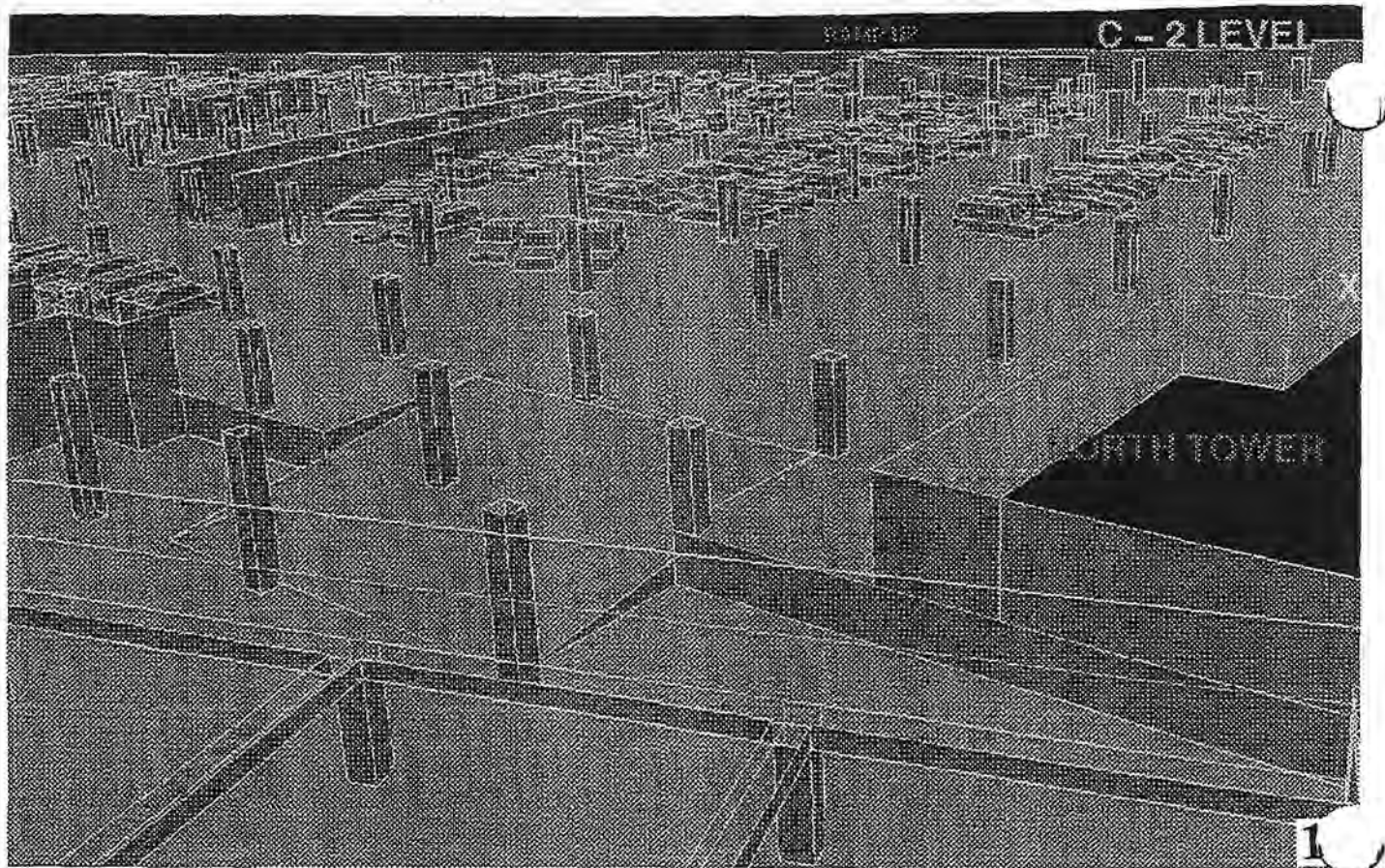
ACKNOWLEDGMENTS

Funding for this research work was provided by the Defense Nuclear Agency. Drs. Michael E. Giltrud and Douglas A. Sunshine served as the technical program monitors. Computer time for these simulations was generously provided by Cray Research Inc. Eagan, MN, the Arctic Region Supercomputer Center at the University of Alaska, Fairbanks, AK, and NASA Ames Research Center. The authors also wish to thank Dr. Kent Goering, Chief, SPSD, DNA, for his support of the program, and Dr. Robin Vermeland of CRI, for his assistance.

REFERENCES

- [1] R. Löhner, K. Morgan, J. Peraire and O.C. Zienkiewicz - Finite Element Methods for High Speed Flows; AIAA-85-1531-CP (1985).
- [2] R. Löhner, K. Morgan, J. Peraire and M. Vahdati - Finite Element Flux-Corrected Transport (FEM-FCT) for the Euler and Navier-Stokes Equations; ICASE Rep. 87-4, *Int. J. Num. Meth. Fluids* 7, 1093-1109 (1987).
- [3] S.T. Zalesak - Fully Multidimensional Flux-Corrected Transport Algorithm for Fluids; *J. Comp. Phys.* 31, 335-362 (1979).
- [4] D.L. Book, J.P. Boris and K. Hain - Flux-corrected Transport. II. Generalizations of the Method; *J. Comp. Phys.* 18, 248 (1975).
- [5] J.P. Boris and D.L. Book - Flux-corrected Transport. III. Minimal-Error FCT Algorithms; *J. Comp. Phys.* 20, 397-431 (1976).
- [6] J.D. Baum and R. Löhner - Numerical Simulation of Shock-Elevated Box Interaction Using an Adaptive Finite Element Shock Capturing Scheme; *AIAA J.* 32, 4, 682-692 (1994).
- [7] J.D. Baum, R. Löhner and E. Loth - Numerical Simulation of Shock Interaction with Complex Geometry Canisters; in *Current Topics in Shock Waves*; American Institute of Physics (Y. Kim ed.), New York (1989).
- [8] R. Löhner and J.D. Baum - Numerical Simulation of Shock Interaction with Complex Geometry Three-Dimensional Structures Using A New Adaptive H-Refinement Scheme on Unstructured Grids; AIAA-90-0700 (1990).
- [9] J.D. Baum and R. Löhner - Numerical Simulation of Shock Interaction with a Modern Main Battle-field Tank; AIAA-91-1666 (1991).
- [10] J.D. Baum and R. Löhner - Numerical Simulation of Three-Dimensional Shock Diffraction Phenomena Using Adaptive, Unstructured Grid Methodology; pp.97-102 in *Proc. 4th Int. Symp. on Comp. Fluid Dyn.* Davis, CA, (1992).
- [11] H. Luo, J.D. Baum, R. Löhner and J. Cabello - Adaptive Edge-Based Finite Element Schemes for the Euler and Navier-Stokes Equations; AIAA-93-0336 (1993).
- [12] H. Luo, J.D. Baum, and R. Löhner - Numerical Solution of the Euler Equations for Complex Aerodynamic Configurations Using an Edge-Based Finite Element Scheme; AIAA-93-2933 (1993).
- [13] H. Luo, J.D. Baum and R. Löhner - Edge-Based Finite Element Scheme for the Euler Equations; *AIAA J.* 32, 6, 1183-1190 (1994).
- [14] E. Mestreau, R. Löhner, and S. Aita, " TGV Tunnel-Entry Simulations Using a Finite Element Code with Automatic Remeshing," *31st Aerospace Sciences Meeting*, Reno, Nevada, January 11-14, 1993.
- [15] R. Löhner and P. Parikh - Three-Dimensional Grid Generation by the Advancing Front Method; *Int. J. Num. Meth. Fluids* 8, 1135-1149 (1988).
- [16] R. Löhner - Finite Elements in CFD: Grid Generation, Adaptivity and Parallelization; Chapter 8 in *AGARD Rep. 787, Proc. Special Course on Unstructured Grid Methods for Advection Dominated Flows*, VKI, Belgium, May and NASA Ames, Moffet Field, CA, September (1992).
- [17] R. Löhner - An Adaptive Finite Element Scheme for Transient Problems in CFD; *Comp. Meth. Appl. Mech. Eng.* 61, 323-338 (1987).
- [18] R. Löhner and J.D. Baum - Adaptive H-Refinement on 3-D Unstructured Grids for Transient Problems; *Int. J. Num. Meth. Fluids* 14, 1407-1419 (1992).
- [19] R. Löhner, P. Parikh and C. Gumbert - Some Algorithmic Problems of Plotting Codes for Unstructured Grids; AIAA-89-1981-CP (1989).





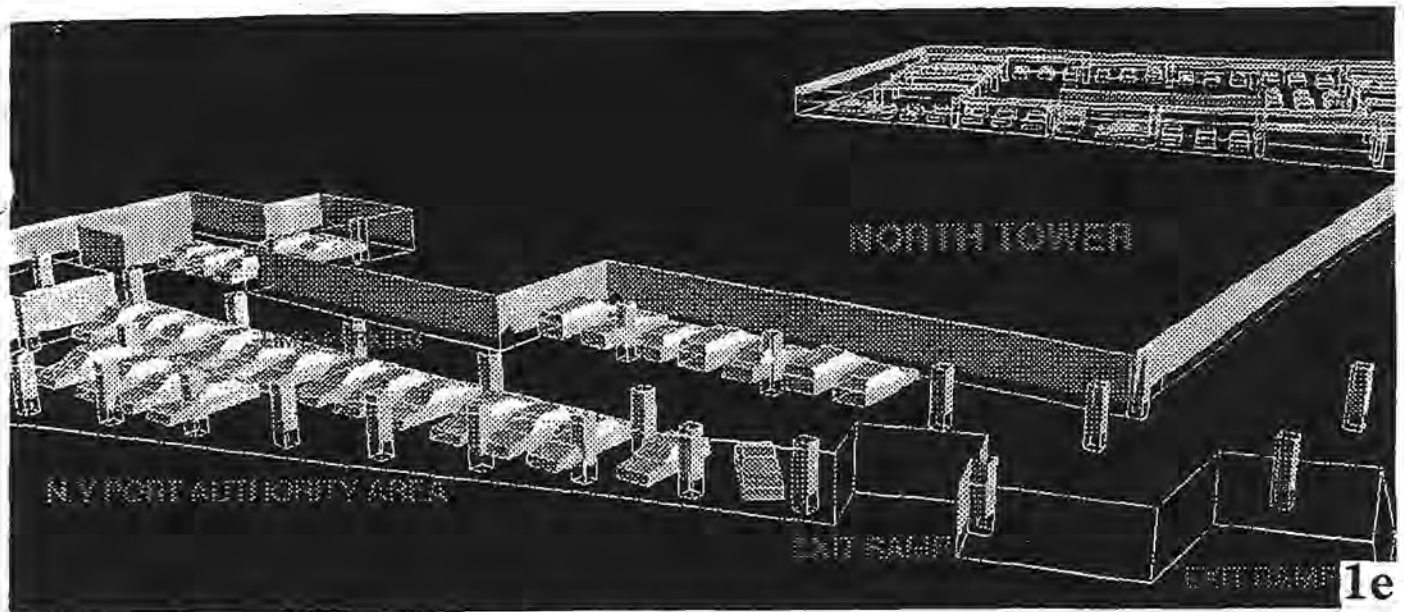


Fig. 1. Geometry Definition of the B-2 Floor, World Trade Center, including Line Formation and Solid Body Descriptions: a) Line Formation, A View from the North; b) The Central and Southern Parking Zones, Including Ramps T and N; c) The Central and Secret Service Parking Zones, Including Ramp S; d) Exit Ramps to West St. and the Central Parking Zone; and e) The New-York Port Authority Area.

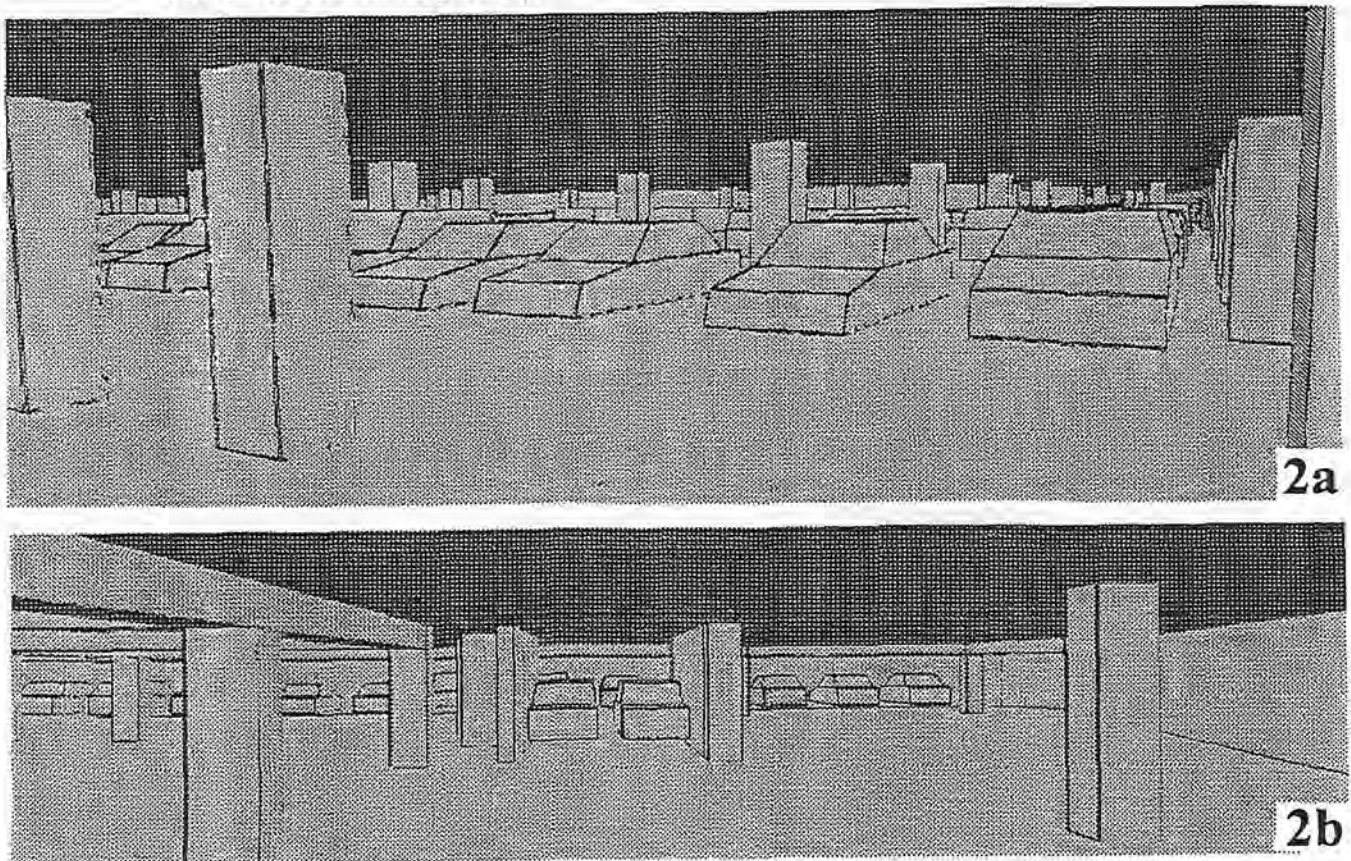


Fig. 2. Snap Shots Taken During the Fly-Through: a) The Central Parking Zone Opposite Blast Point; and b) The Secret Service Area and the Presidential Limousines.

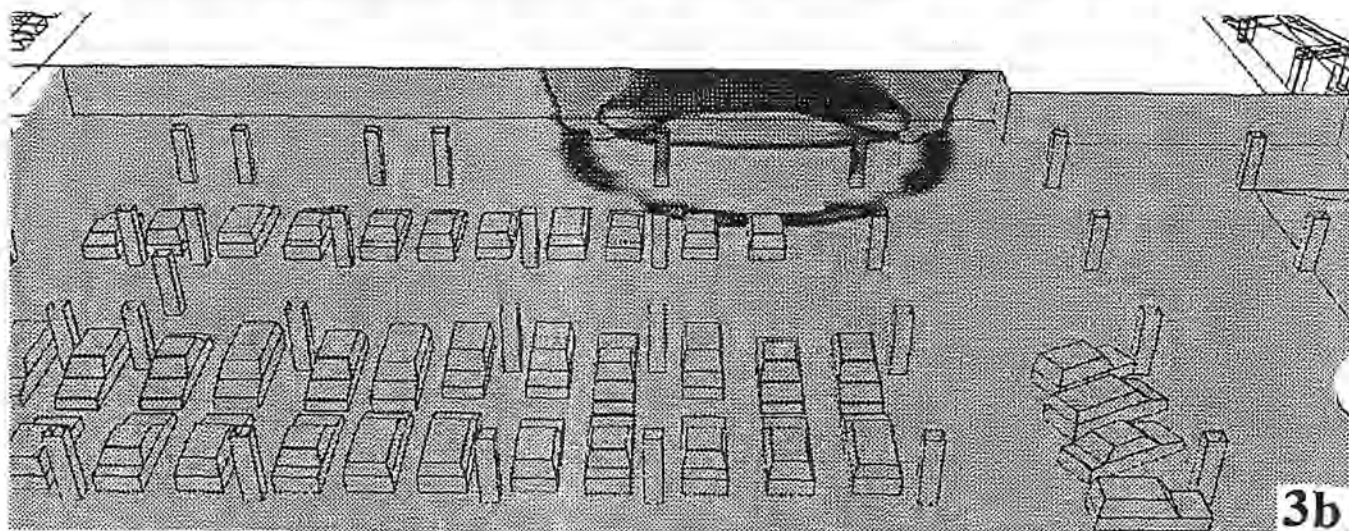
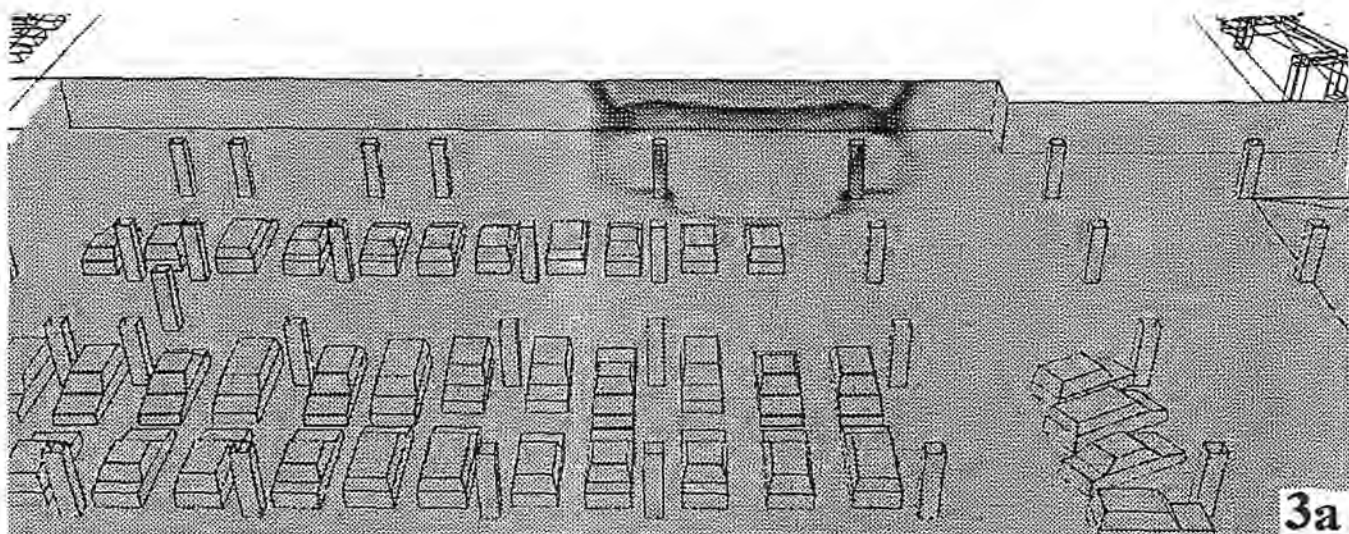
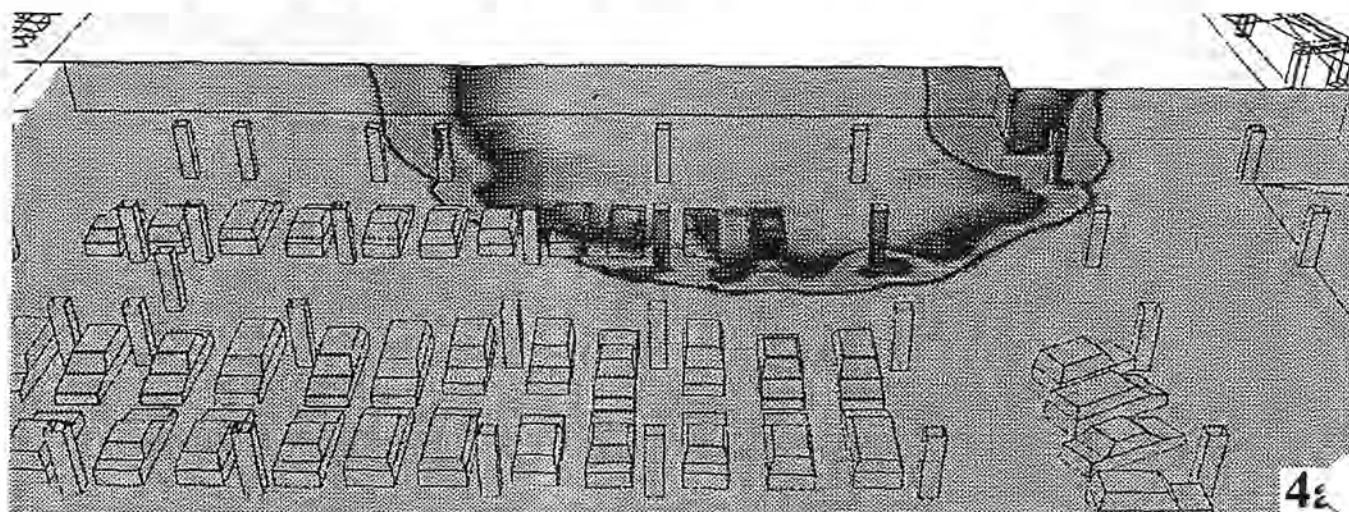


Fig. 3. Expanded Views of Pressure Contours in the Near-Blast Zone During the Early Stages: a) $t=3.63$ ms, Peak Pressure=1513.35 psi; and b) $t=5.25$ ms, Peak Pressure=477.0 psi.



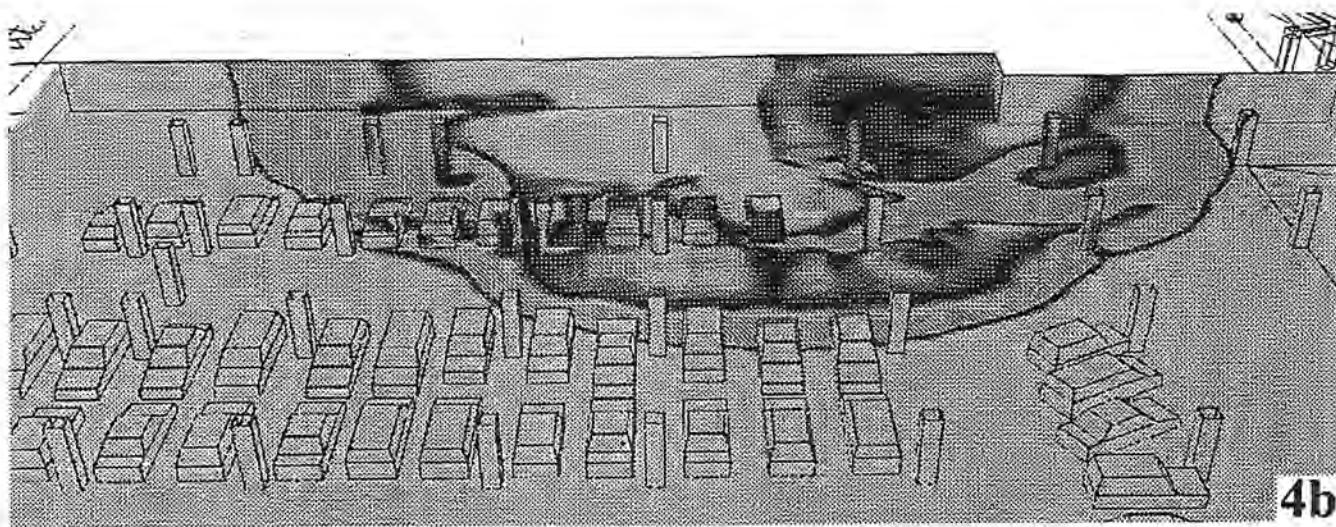


Fig. 4. Expanded Views of Pressure Contours in the Near-Blast Zone at:
a) $t=12.51$ ms, Peak Pressure=103.03 psi; and b) $t=19.49$ ms, Peak Pressure=38.37 psi.

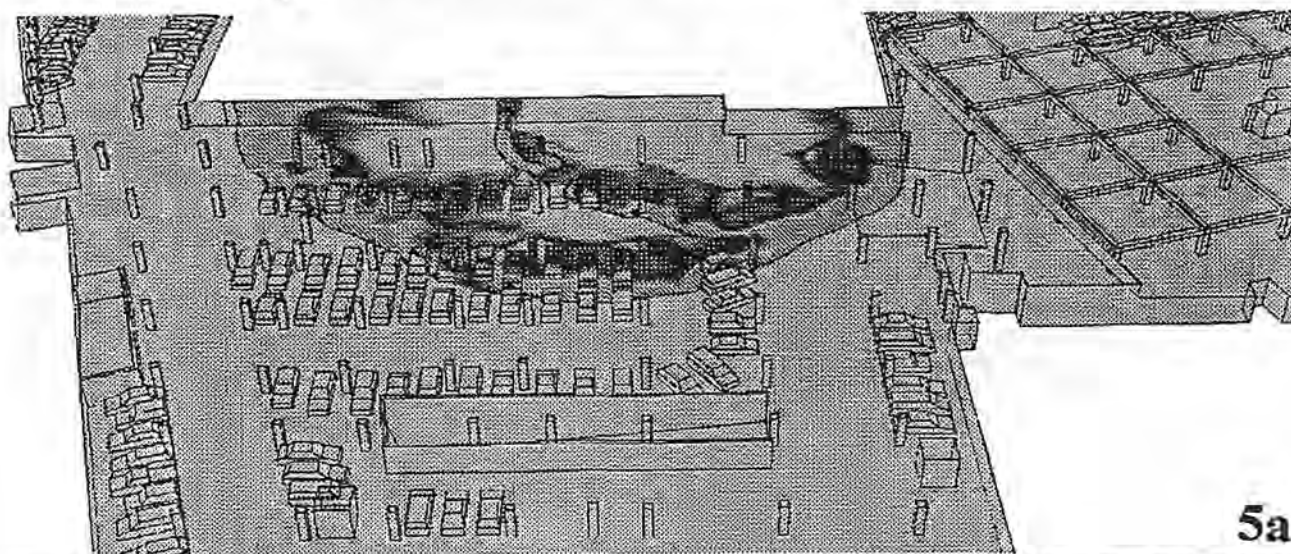


Fig. 5. Expanded Views of Pressure Contours in the Mid-Zone at:
a) $t=29.04$ ms, Peak Pressure=33.51 psi; and b) $t=34.45$ ms, Peak Pressure=41.47 psi.

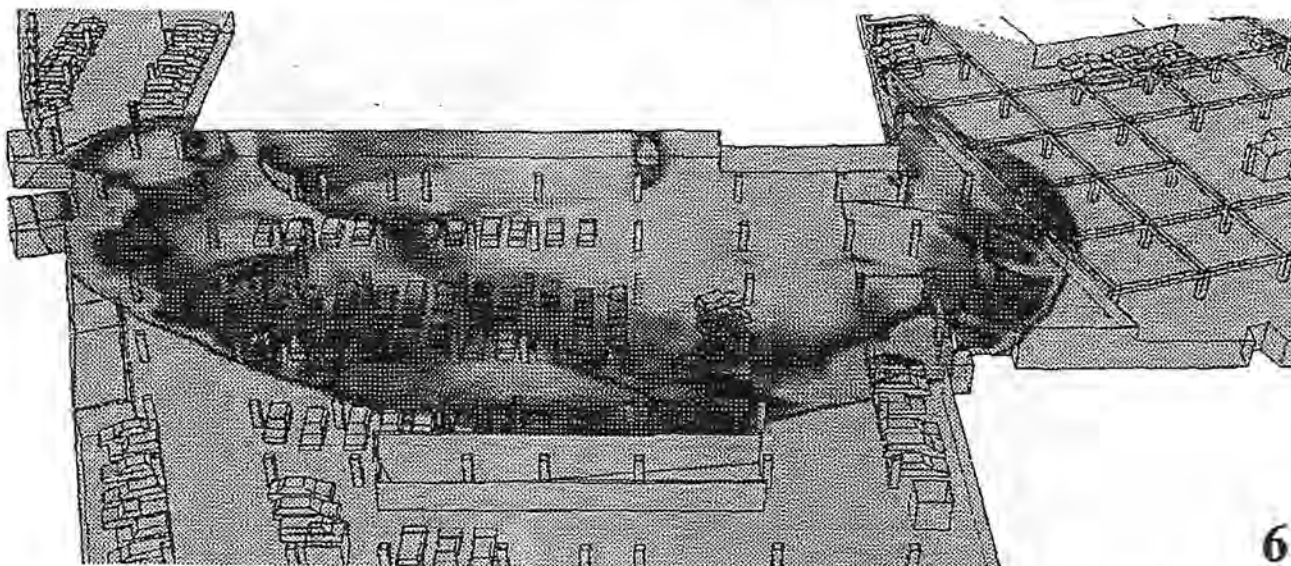
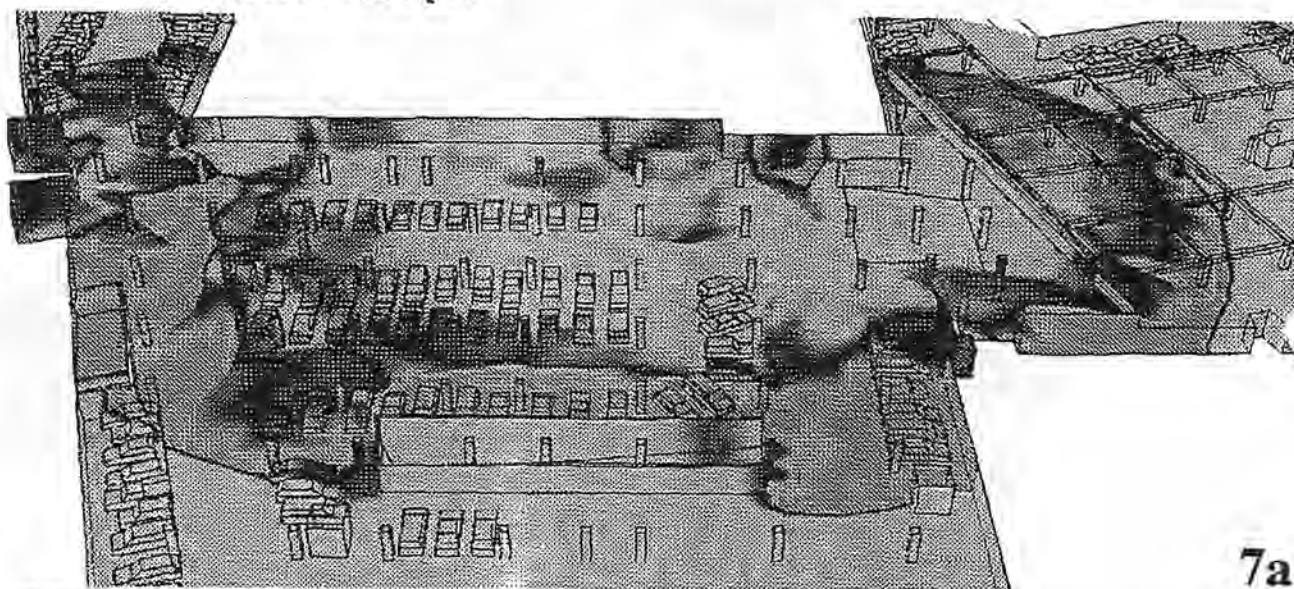
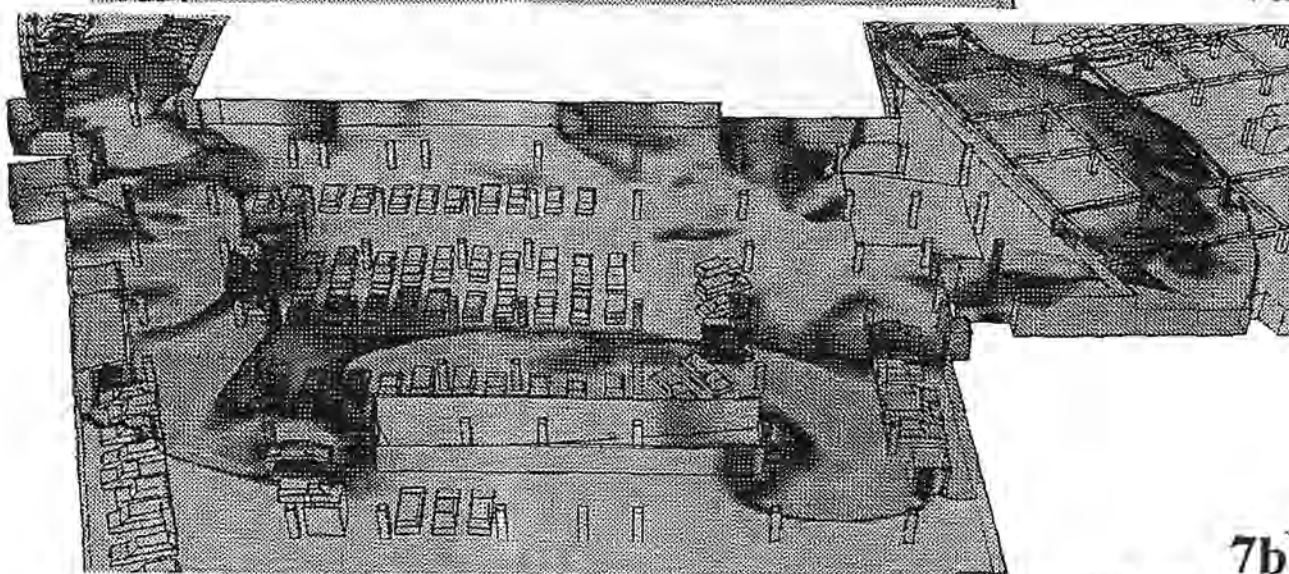


Fig. 6. Expanded View of Pressure Contours in the Mid-Zone at $t=59.48$ ms, Peak Pressure ≈ 74.58 psi.



7a



7b

Fig. 7. Expanded Views of Pressure Contours in the Mid-Zone at: a) $t=89.55$ ms, Peak Pressure $= 10.46$ psi; and b) $t=95.81$ ms, Peak Pressure $= 10.37$ psi.

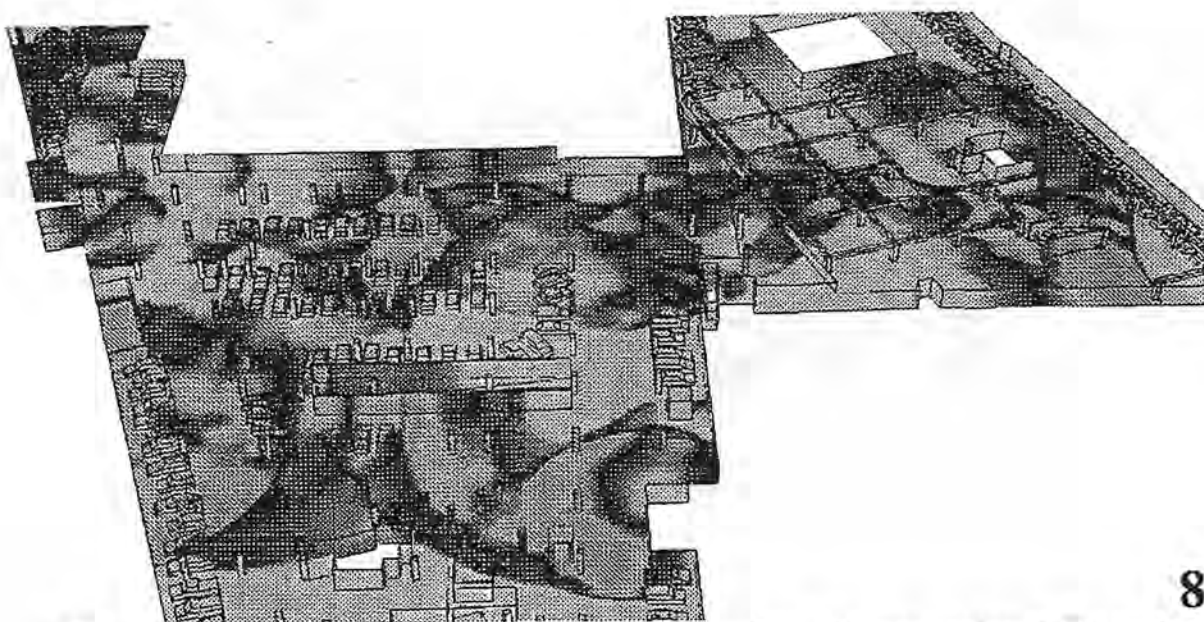
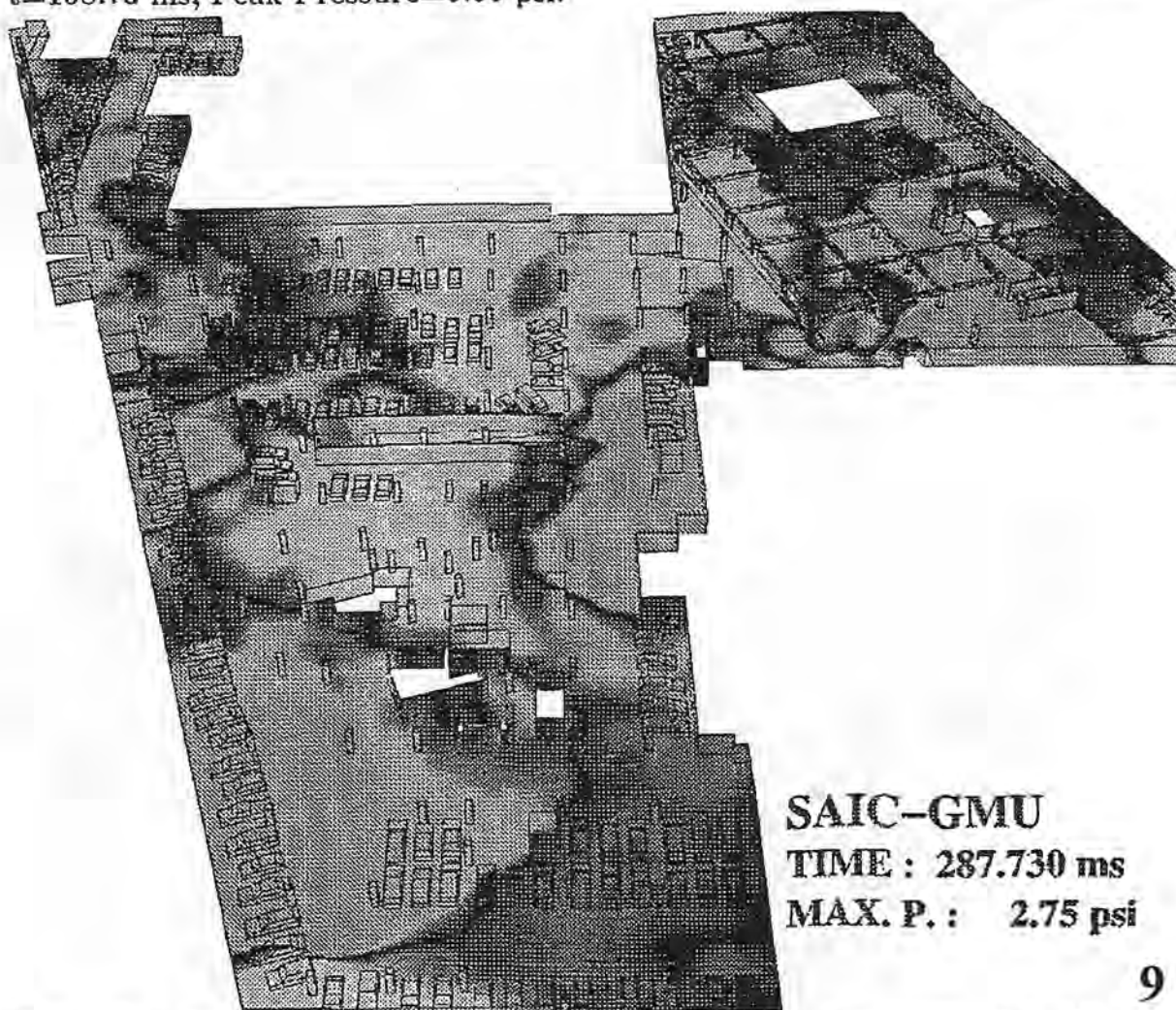


Fig. 8. Pressure Contours in the Complete Computational Domain at $t=158.73$ ms, Peak Pressure=5.99 psi.



SAIC-GMU
TIME : 287.730 ms
MAX. P. : 2.75 psi

Fig. 9. Pressure Contours in the Complete Computational Domain at $t=287.73$ ms, Peak Pressure=2.75 psi.